

Hyperspectral Pansharpening Using Noisy Panchromatic Image

Saori Takeyama^{*†}, Shunsuke Ono^{*} and Itsuo Kumazawa^{*}

^{*} Tokyo Institute of Technology, Kanagawa, Japan

[†] E-mail: takeyama.s.aa@m.titech.ac.jp Tel: +81-45-924-5089

Abstract—Capturing high-resolution hyperspectral (HS) images is very difficult. To solve this problem, hyperspectral pansharpening techniques have been widely studied. These techniques estimate an HS image of high spatial and spectral resolution (high HS image) from a pair of an observed low resolution HS image (low HS image) and an observed high resolution panchromatic (observed PAN) image. Given HS and PAN images often contain noise, but most of the existing methods would not consider it, so that the results have artifacts, noise and spectral distortion in such a situation. To tackle this issue, we propose a new hyperspectral pansharpening method considering noise in both given HS and PAN images. Our method estimates not only a high HS image but also a clean PAN image simultaneously, leading to high quality and robust estimation. The proposed method effectively exploits observed information and a-priori knowledge, and it is reduced to a nonsmooth convex optimization problem, which is efficiently solved by a primal-dual splitting method. Our experiments demonstrate the advantages of our method over existing hyperspectral pansharpening methods.

I. INTRODUCTION

A hyperspectral (HS) image has 1D spectral information in addition to 2D spatial information, which contains rich information, e.g., information on invisible light and narrow wavelength interval. Since it can visualize the intrinsic characteristics of scene objects and environmental lighting, hyperspectral imaging is a promising research topic and offers many applications in a wide range of fields, e.g., remote sensing, agriculture and biomedical engineering [1], [2]. These applications require an HS image of high spatial and spectral resolution (high HS image). However, since the amount of incident energy is limited, and there are critical tradeoffs between the spatial resolution and the spectral resolution of HS imaging systems, it is a very difficult task to capture a high HS image.

Hyperspectral pansharpening techniques [3], [4] try to resolve this dilemma, and have been actively studied [5]–[16]. They estimate a high HS image using a pair of an observed HS image of high spectral resolution but low spatial resolution (low HS image) and an observed high spatial resolution panchromatic image (observed PAN image), where a PAN image has only 2D spatial information, i.e., a gray scale image.

Most of recent hyperspectral pansharpening methods [12]–[16] utilize a-priori knowledge on an HS image and observed information on a low HS image and an observed PAN image, and estimate high HS images by solving optimization problems. These methods can estimate better HS images than traditional pansharpening methods. In addition, the method

proposed in [16] considers a noisy low HS image and effectively uses a-priori knowledge, which are spatial and spectral smoothness, so that it can estimate a high HS image without artifacts and spectral distortion. However, since these methods do not consider that an observed PAN image may also contains noise, they cannot achieve high quality estimation, when the observed PAN image is noisy, and thus the resulting HS images often have artifacts and spectral distortion.

To resolve the above problems, we propose a new robust hyperspectral pansharpening method, which considers noisy observed HS and PAN images. The proposed method estimates not only a high HS image but also a clean PAN image, leading to high quality and robust estimation. The method is built upon a convex optimization problem, where its objective function consists of regularization terms for HS and PAN images, respectively, and an edge similarity term between HS and PAN images. Data-fidelity to a low HS and an observed PAN image and their dynamic ranges are evaluated by hard constraints. This problem fully utilizes observed information and a-priori knowledge of an HS and a PAN image, so that it can estimate a high HS image without artifacts and spectral distortion even if both observed images are contaminated by severe noise. To solve the optimization problem, we adopt a primal-dual splitting method [17], which is a proximal splitting algorithm and has been successfully applied to image restoration [18]–[21]. Experimental results on hyperspectral pansharpening illustrate superior performance of the proposed method compared with existing hyperspectral pansharpening methods.

II. PROPOSED METHOD

A. Observation Model

Let $\bar{\mathbf{u}} \in \mathbb{R}^{NB}$ be a true high HS image with N pixels and B spectral bands. In hyperspectral pansharpening, a low HS image \mathbf{v} and an observed PAN image \mathbf{p} are assumed to be given with the observation model:

$$\mathbf{v} = \mathbf{S}\mathbf{B}\bar{\mathbf{u}} + \mathbf{n}_1 \in \mathbb{R}^{\frac{NB}{r}}, \quad (1)$$

$$\mathbf{p} = \mathbf{R}\bar{\mathbf{u}} + \mathbf{n}_2 \in \mathbb{R}^N, \quad (2)$$

where $\mathbf{S} \in \mathbb{R}^{\frac{NB}{r} \times NB}$ is a downsampling matrix with a downsampling rate of r (r is divisor of N), \mathbf{B} is a blur matrix, \mathbf{n}_1 and \mathbf{n}_2 are additive white Gaussian noises with standard deviations σ_1 and σ_2 , respectively, and $\mathbf{R} \in \mathbb{R}^{N \times NB}$ is a matrix representing the spectral response of the observed

PAN image (\mathbf{R} calculates weighted average along the spectral direction). In general, since HS images contain more noise than PAN images, we assume $\sigma_1 > \sigma_2$. This model says that both the low HS image and the observed PAN image contain considerable noise, which is a natural situation in hyperspectral imaging.

B. Problem Formulation

Based on the model in Sec. II-A, we formulate a hyperspectral pansharpening problem as a convex optimization problem. This problem estimates not only a high HS image $\mathbf{u} \in \mathbb{R}^{NB}$ but also a clean PAN image $\mathbf{q} \in \mathbb{R}^N$, leading to high quality and robust estimation.

$$\begin{aligned} & \min_{\mathbf{u}, \mathbf{q}} \text{HSSTV}(\mathbf{u}) + \lambda \|\mathbf{D}\mathbf{u} - \mathbf{D}\mathbf{M}\mathbf{q}\|_{1,2} + \|\mathbf{D}\mathbf{q}\|_{1,2} \\ & \text{s.t.} \quad \begin{cases} \mathbf{S}\mathbf{B}\mathbf{u} \in \mathcal{B}_{2,\varepsilon}^{\mathbf{v}} := \{\mathbf{x} \in \mathbb{R}^{\frac{NB}{r}} \mid \|\mathbf{x} - \mathbf{v}\|_2 \leq \varepsilon\}, \\ \mathbf{q} \in \mathcal{B}_{2,\eta}^{\mathbf{p}} := \{\mathbf{x} \in \mathbb{R}^N \mid \|\mathbf{x} - \mathbf{p}\|_2 \leq \eta\}, \\ \mathbf{u} \in [\mu_{\min}, \mu_{\max}]^{NB}, \\ \mathbf{q} \in [0, 1]^N, \end{cases} \end{aligned} \quad (3)$$

where $\mathbf{D} = (\mathbf{D}_v^T \mathbf{D}_h^T)^T \in \mathbb{R}^{2NB \times NB}$ is a spatial difference operator with \mathbf{D}_v and \mathbf{D}_h being vertical and horizontal difference operators, respectively, $\|\cdot\|_{1,2}$ is the mixed $\ell_{1,2}$ norm, which calculates the ℓ_2 norm of spatial difference values of each pixel, and the ℓ_1 norm of them after that. In Prob. (3), the parameter $\lambda > 0$ is the parameter adjusting evaluation degree of the second term, and $\mathbf{M} \in \mathbb{R}^{NB \times N}$ is a linear operator that replicates the estimated PAN image B times along the spectral direction.

The first term in Prob. (3) is a regularization function for HS image restoration named as hybrid spatio-spectral total variation (HSSTV). This regularization function simultaneously evaluates both the spatio-spectral piecewise smoothness and the direct spatial piecewise smoothness of an HS image. In [22], HSSTV is defined by

$$\text{HSSTV}(\mathbf{u}) := \left\| \begin{bmatrix} \mathbf{D}\mathbf{D}_b\mathbf{u} \\ \omega\mathbf{D}\mathbf{u} \end{bmatrix} \right\|_{1,p} =: \|\mathbf{A}_\omega\mathbf{u}\|_{1,p}, \quad (4)$$

where \mathbf{D}_b is a spectral difference operator, ω is a parameter balancing between the spatio-spectral piecewise smoothness $\mathbf{D}\mathbf{D}_b\mathbf{u}$ and the direct spatial piecewise smoothness $\mathbf{D}\mathbf{u}$, and $\|\cdot\|_{1,p}$ is the mixed $\ell_{1,p}$ norm with $p = 1$ or 2 . HSSTV is our previous work, and it has been shown to be very effective in HS image restoration. By using HSSTV, the proposed hyperspectral pansharpening method can do robust estimation when the low HS image and the observed PAN image contain noise.

The second term in Prob. (3) evaluates edge similarity between the high HS image \mathbf{u} and the estimated PAN image \mathbf{q} , which is originally proposed in [23]. Specifically, we can assume that the non-zero differences of the high HS image are sparse and correspond to edges, and that their positions should be the same as those of the estimated PAN image. Hence, evaluating their errors by the mixed $\ell_{1,2}$ norm is a reasonable approach for exploiting the spatial information on the estimated PAN image.

The first constraint in (3) serves as data-fidelity to the low HS image \mathbf{v} and is defined as the \mathbf{v} -centered ℓ_2 -norm ball with the radius $\varepsilon > 0$. Likewise, the second constraint in (3) plays data-fidelity role to the observed PAN image \mathbf{p} and is defined as the \mathbf{p} -centered ℓ_2 -norm ball with the radius $\eta > 0$. As mentioned in [16], [22], [24]–[27], such a hard constraint facilitates the parameter setting because ε and η have a clear meaning. The third and fourth constraint in (3) represent the dynamic range of a HS image and a PAN image with $\mu_{\min} < \mu_{\max}$, respectively.

C. Optimization

Since Prob. (3) is a convex but highly constrained nonsmooth optimization problem, we require a suitable iterative algorithm, e.g., an alternating direction method of multipliers, to solve it. In this paper, we adopt a primal-dual splitting method [17]. It can solve convex optimization problems of the form:

$$\min_{\mathbf{u}} g(\mathbf{u}) + h(\mathbf{L}\mathbf{u}), \quad (5)$$

where g and h are proper lower semicontinuous convex functions and *proximable*, i.e., the proximity operators [28] of g and h are computable, and \mathbf{L} is a linear operator. Here, the proximity operator of a proper lower semicontinuous convex function f is defined as follows: for $\gamma > 0$,

$$\text{prox}_{\gamma f}(\mathbf{x}) := \underset{\mathbf{y}}{\text{argmin}} f(\mathbf{y}) + \frac{1}{2\gamma} \|\mathbf{y} - \mathbf{x}\|_2^2.$$

Since the primal-dual splitting method can solve a problem as long as it satisfy (5), we utilize this method for nonsmooth optimization problem.

When above condition is satisfied, the algorithm solving Prob. (5) is given by

$$\begin{cases} \mathbf{u}^{(n+1)} = \text{prox}_{\gamma_1 g}(\mathbf{u}^{(n)} - \gamma_1 \mathbf{L}^T \mathbf{y}^{(n)}), \\ \mathbf{y}^{(n+1)} = \text{prox}_{\gamma_2 h^*}(\mathbf{y}^{(n)} + \gamma_2 \mathbf{L}(2\mathbf{u}^{(n+1)} - \mathbf{u}^{(n)})), \end{cases}$$

where $\gamma_1, \gamma_2 > 0$ are stepsizes of the primal-dual splitting method, which satisfy $\gamma_1 \gamma_2 (\sigma_1(\mathbf{L}))^2 \leq 1$ ($\sigma_1(\mathbf{L})$ is the largest singular value of \mathbf{L}). The function h^* is the convex conjugate of h , and the proximity operator of h^* is available via that of h [29, Theorem 14.3(ii)] as follows:

$$\text{prox}_{\gamma h^*}(\mathbf{x}) = \mathbf{x} - \gamma \text{prox}_{\frac{1}{\gamma} h}\left(\frac{1}{\gamma} \mathbf{x}\right). \quad (6)$$

To solve it by the primal-dual splitting method, we reformulate Prob. (3) into Prob. (5).

First, to put the four constraints in Prob. (3) into the objective function, we introduce the indicator functions of them. The indicator function of a nonempty closed convex set C is defined by

$$\iota_C(\mathbf{x}) := \begin{cases} 0, & \text{if } \mathbf{x} \in C, \\ \infty, & \text{otherwise.} \end{cases} \quad (7)$$

Then, Prob. (3) can be rewritten as

$$\min_{\mathbf{u}, \mathbf{q}} \|\mathbf{A}_\omega\mathbf{u}\|_{1,p} + \lambda \|\mathbf{D}\mathbf{u} - \mathbf{D}\mathbf{M}\mathbf{q}\|_{1,2} + \|\mathbf{D}\mathbf{q}\|_{1,2}$$

$$+ \iota_{\mathcal{B}_{2,\varepsilon}^{\mathbf{y}}}(\mathbf{S}\mathbf{B}\mathbf{u}) + \iota_{\mathcal{B}_{2,\eta}^{\mathbf{p}}}(\mathbf{q}) + \iota_{[\mu_{\min}, \mu_{\max}]^{NB}}(\mathbf{u}) + \iota_{[0,1]^N}(\mathbf{q}). \quad (8)$$

Because of (7), Prob. (3) and Prob. (8) are equivalent.

Then, by letting

$$\begin{aligned} g: \mathbb{R}^{N(B+1)} &\rightarrow \mathbb{R}^2: (\mathbf{u}, \mathbf{q}) \mapsto (\iota_{[\mu_{\min}, \mu_{\max}]^{NB}}(\mathbf{u}), \iota_{[0,1]^N}(\mathbf{q})) \\ h: \mathbb{R}^{((6+\frac{1}{r})B+3)^N} &\rightarrow \mathbb{R} \cup \{\infty\}: (\mathbf{y}_1, \mathbf{y}_2, \mathbf{y}_3, \mathbf{y}_4, \mathbf{y}_5) \mapsto \\ &\|\mathbf{y}_1\|_{1,p} + \lambda \|\mathbf{y}_2\|_{1,2} + \|\mathbf{y}_3\|_{1,2} + \iota_{\mathcal{B}_{2,\varepsilon}^{\mathbf{y}}}(\mathbf{y}_4) + \iota_{\mathcal{B}_{2,\eta}^{\mathbf{p}}}(\mathbf{y}_5), \\ \mathbf{L}: \mathbb{R}^{N(B+1)} &\rightarrow \mathbb{R}^{((6+\frac{1}{r})B+3)^N}: \\ (\mathbf{u}, \mathbf{q}) &\mapsto (\mathbf{A}_\omega \mathbf{u}, \mathbf{D}\mathbf{u} - \mathbf{D}\mathbf{M}\mathbf{q}, \mathbf{D}\mathbf{q}, \mathbf{S}\mathbf{B}\mathbf{u}, \mathbf{q}), \end{aligned}$$

Prob. (8) is reduced to Prob. (5). Using (6), the resulting algorithm for solving (3) is summarized in Algorithm 1.

We explain how to calculate the proximity operator of the indicator function of C . This proximity operator equals the metric projection onto C , which is characterized by

$$P_C(\mathbf{x}) = \underset{\mathbf{z}}{\operatorname{argmin}} \|\mathbf{z} - \mathbf{x}\|_2 \text{ s.t. } \mathbf{z} \in C.$$

The proximity operators in steps 2 and 12 can be computed as follows: for $i = 1, \dots, NB$,

$$\begin{aligned} [\operatorname{prox}_{\gamma \iota_{[\mu_{\min}, \mu_{\max}]^{NB}}}(\mathbf{x})]_i &= [P_{[\mu_{\min}, \mu_{\max}]^{NB}}(\mathbf{x})]_i \\ &= \min\{\max\{x_i, \mu_{\min}\}, \mu_{\max}\}, \end{aligned} \quad (9)$$

$$\operatorname{prox}_{\gamma \iota_{\mathcal{B}_{2,\varepsilon}^{\mathbf{y}}}}(\mathbf{x}) = P_{\mathcal{B}_{2,\varepsilon}^{\mathbf{y}}}(\mathbf{x}) = \begin{cases} \mathbf{x}, & \text{if } \mathbf{x} \in \mathcal{B}_{2,\varepsilon}^{\mathbf{y}}, \\ \mathbf{v} + \frac{\varepsilon(\mathbf{x}-\mathbf{v})}{\|\mathbf{x}-\mathbf{v}\|_2}, & \text{otherwise.} \end{cases} \quad (10)$$

For step 3, one can calculate $\operatorname{prox}_{[0,1]^N}(\mathbf{x})$ by substituting 0, 1, and N for μ_{\min} , μ_{\max} and NB in (9), respectively. Likewise, for step 13, \mathbf{p} and η are substituted for \mathbf{v} and ε in (10), respectively, so that $\operatorname{prox}_{\mathcal{B}_{2,\eta}^{\mathbf{p}}}(\mathbf{x})$ can be computed.

The proximity operators of the ℓ_1 norm and the mixed $\ell_{1,2}$ norm in steps 6 and 7 are reduced to simple soft-thresholding type operations: for $\gamma > 0$ and $i = 1, \dots, 2n$,

$$\begin{aligned} [\operatorname{prox}_{\gamma \|\cdot\|_1}(\mathbf{x})]_i &= \operatorname{sgn}(x_i) \max\{|x_i| - \gamma, 0\}, \\ [\operatorname{prox}_{\gamma \|\cdot\|_{1,2}}(\mathbf{x})]_i &= \max\left\{1 - \gamma \left(\sum_{j=0}^1 x_{i+jn}^2\right)^{-\frac{1}{2}}, 0\right\} x_i, \end{aligned}$$

where n is the number of pixels in a target image, i.e., $n = NB$ and N for the high HS image \mathbf{u} and the estimated PAN image \mathbf{q} , respectively, sgn is the sign function, and $\hat{i} := ((i-1) \bmod n) + 1$.

III. EXPERIMENTS

We demonstrate the advantages of the proposed method over existing hyperspectral pansharpening methods. In this experiments, we generated a pair of a low HS and an observed PAN image based on (1) and (2), estimated the high HS image from the pair using each method, and evaluated the estimated high HS images based on four standard quality measures: Cross Correlation (CC), the Spectral Angle Mapper (SAM) [30], the Root Mean Squared Error (RMSE) and Erreur Relative Globale Adimensionnelle de synthèse (ERGAS) [31].

Algorithm 1: A primal-dual splitting method for Prob. (3).

```

input :  $\mathbf{u}^{(0)}, \mathbf{q}^{(0)}, \mathbf{y}_1^{(0)}, \mathbf{y}_2^{(0)}, \mathbf{y}_3^{(0)}, \mathbf{y}_4^{(0)}, \mathbf{y}_5^{(0)}$ 
1 while A stopping criterion is not satisfied do do
2    $\mathbf{u}^{(n+1)} = \operatorname{prox}_{\gamma_1 \iota_{[\mu_{\min}, \mu_{\max}]^{NB}}}(\mathbf{u}^{(n)} - \gamma_1 (\mathbf{A}_\omega^\top \mathbf{y}_1^{(n)} +$ 
       $\mathbf{D}^\top \mathbf{y}_2^{(n)} + \mathbf{B}^\top \mathbf{S}^\top \mathbf{y}_4^{(n)}));$ 
3    $\mathbf{q}^{(n+1)} =$ 
       $\operatorname{prox}_{\gamma_1 \iota_{[0,1]^N}}(\mathbf{q}^{(n)} - \gamma_1 (-\mathbf{M}^\top \mathbf{D}^\top \mathbf{y}_2^{(n)} + \mathbf{D}^\top \mathbf{y}_3^{(n)} + \mathbf{y}_5^{(n)}));$ 
4    $\mathbf{y}_1^{(n)} \leftarrow \mathbf{y}_1^{(n)} + \gamma_2 \mathbf{A}_\omega (2\mathbf{u}^{(n+1)} - \mathbf{u}^{(n)});$ 
5    $\mathbf{y}_2^{(n)} \leftarrow$ 
       $\mathbf{y}_2^{(n)} + \gamma_2 (\mathbf{D}(2\mathbf{u}^{(n+1)} - \mathbf{u}^{(n)}) - \mathbf{D}\mathbf{M}(2\mathbf{q}^{(n+1)} - \mathbf{q}^{(n)}));$ 
6    $\mathbf{y}_3^{(n)} \leftarrow \mathbf{y}_3^{(n)} + \gamma_2 \mathbf{D}(2\mathbf{q}^{(n+1)} - \mathbf{q}^{(n)});$ 
7    $\mathbf{y}_4^{(n)} \leftarrow \mathbf{y}_4^{(n)} + \gamma_2 \mathbf{S}\mathbf{B}(2\mathbf{u}^{(n+1)} - \mathbf{u}^{(n)});$ 
8    $\mathbf{y}_5^{(n)} \leftarrow \mathbf{y}_5^{(n)} + \gamma_2 (2\mathbf{q}^{(n+1)} - \mathbf{q}^{(n)});$ 
9    $\mathbf{y}_1^{(n+1)} = \mathbf{y}_1^{(n)} - \gamma_2 \operatorname{prox}_{\frac{1}{\gamma_2}, \|\cdot\|_1, p} \left( \frac{\mathbf{y}_1^{(n)}}{\gamma_2} \right);$ 
10   $\mathbf{y}_2^{(n+1)} = \mathbf{y}_2^{(n)} - \gamma_2 \operatorname{prox}_{\frac{\lambda}{\gamma_2}, \|\cdot\|_{1,2}} \left( \frac{\mathbf{y}_2^{(n)}}{\gamma_2} \right);$ 
11   $\mathbf{y}_3^{(n+1)} = \mathbf{y}_3^{(n)} - \gamma_2 \operatorname{prox}_{\frac{1}{\gamma_2}, \|\cdot\|_{1,2}} \left( \frac{\mathbf{y}_3^{(n)}}{\gamma_2} \right);$ 
12   $\mathbf{y}_4^{(n+1)} = \mathbf{y}_4^{(n)} - \gamma_2 \operatorname{prox}_{\frac{1}{\gamma_2}, \mathcal{B}_{2,\varepsilon}^{\mathbf{y}}} \left( \frac{\mathbf{y}_4^{(n)}}{\gamma_2} \right);$ 
13   $\mathbf{y}_5^{(n+1)} = \mathbf{y}_5^{(n)} - \gamma_2 \operatorname{prox}_{\frac{1}{\gamma_2}, \mathcal{B}_{2,\eta}^{\mathbf{p}}} \left( \frac{\mathbf{y}_5^{(n)}}{\gamma_2} \right);$ 
14   $n \leftarrow n + 1;$ 

```

We used a Moffett field dataset as the true high HS image, which it is clipped in a region of size $256 \times 128 \times 176$ and normalized its dynamic range into $[0, 1]$, i.e., $\mu_{\min} = 0$ and $\mu_{\max} = 1$ in Prob. (3). In (1) and (2), the downsampling rate of \mathbf{S} was set as $r = 4$, \mathbf{B} was set to a 9×9 Gaussian blur matrix, and \mathbf{R} was set to an weighted-average matrix with its weights w_i ($i = 1, \dots, B$) were defined by

$$w_i = \begin{cases} 1, & \text{if } 1 \leq i \leq 41 \\ 0, & \text{otherwise.} \end{cases}$$

Then, we experimented with three pair of the standard deviations, $(\sigma_1, \sigma_2) = (0.1, 0.025), (0.1, 0.05), (0.1, 0.075)$. The above procedures follow Wald's protocol [32], so that one can see that it is a standard quality assessment methodology of hyperspectral pansharpening.

As compared methods, we utilize 11 existing methods: SFIM [11], MTF-GLP [9], MTF-GLP-HPM [10], GS [7], GSA [8], PCA [5], GFPCA [6], CNMF [15], Bayesian Naive [12], Bayesian Sparse [13] and HySure [14]. To set all parameters of these methods other than HySure, we used setting in a MATLAB toolbox of hyperspectral pansharpening¹. For HySure, we set its hyperparameter as $\lambda_\phi = 0.1\sigma_1$ to enhance its performance, and other parameters were set in the same way with other methods. For our method, the parameters ε and η in (3) were set to oracle value, i.e., $\varepsilon = \|\mathbf{v} - \mathbf{S}\mathbf{B}\mathbf{u}\|_2$, $\eta = \|\mathbf{p} - \mathbf{R}\mathbf{u}\|_2$. Moreover, we varied $\lambda \in [0.01, 0.1]$ and $\omega \in [0, 0.1]$ to inspect suitable them. We set the stepsizes, the max iteration number and the stopping criterion of the primal-

¹<http://openremotesensing.net/>

TABLE I
QUALITY MEASURES FOR $\sigma = 0.05$ (LEFT) AND $\sigma = 0.1$ (RIGHT).

method	$\sigma_2 = 0.025$				$\sigma_2 = 0.05$				$\sigma_2 = 0.075$			
	CC	SAM	RMSE	ERGAS	CC	SAM	RMSE	ERGAS	CC	SAM	RMSE	ERGAS
SFIM [11]	0.4528	38.87	1571	23.86	0.4170	39.45	1691	25.32	0.4259	39.59	1680	25.63
MTF-GLP [9]	0.6920	34.68	974.4	16.05	0.6284	35.47	1112	17.76	0.5826	36.03	1210	18.92
MTF-GLP-HPM [10]	0.4605	38.89	1576	23.80	0.4286	39.54	1680	25.11	0.4429	39.57	1643	25.25
GS [7]	0.5946	39.77	1101	20.54	0.5108	41.04	1213	22.39	0.4310	42.00	1311	24.02
GSA [8]	0.6841	41.71	1083	20.11	0.6201	44.77	1303	23.81	0.5459	48.48	1601	28.89
PCA [5]	0.5913	39.93	1111	20.72	0.5086	41.21	1221	22.53	0.4297	42.17	1317	24.13
GFPCA [6]	0.9019	11.18	462.1	8.045	0.8813	11.54	500.6	8.762	0.8694	11.71	520.2	9.138
CNMF [15]	0.8863	15.10	512.1	8.338	0.7839	16.23	729.0	11.90	0.6811	17.69	951.5	15.48
Bayesian Naive [12]	0.8498	27.20	602.2	11.07	0.7782	30.88	800.9	14.26	0.6920	35.00	1052	18.38
Bayesian Sparse [13]	0.8526	26.68	594.1	10.95	0.7830	30.34	785.4	14.03	0.7003	34.35	1023	17.93
HySure [14]	0.9273	15.93	402.9	7.017	0.8704	20.46	557.1	9.714	0.7868	25.34	774	13.52
proposed (ℓ_1)	0.9515	9.777	322.4	5.672	0.9409	9.891	344.4	6.135	0.9350	9.919	356.7	6.387
proposed ($\ell_{1,2}$)	0.9516	9.763	322.2	5.666	0.9410	9.878	344.2	6.130	0.9351	9.907	356.5	6.382

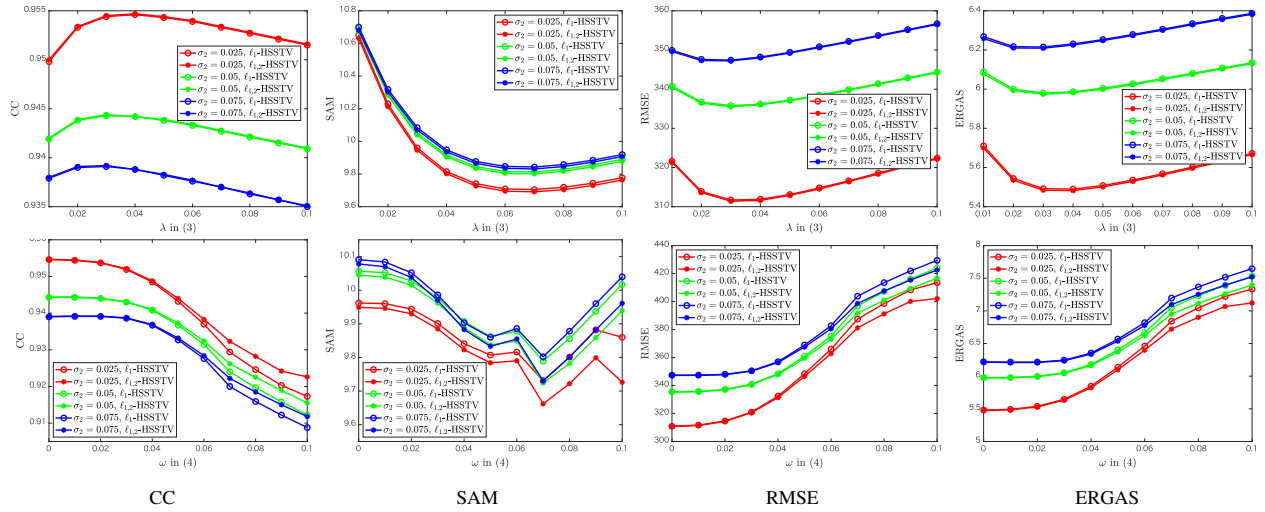


Fig. 1. Quality measures versus λ in (3) (top) / ω in (4) (bottom).

dual splitting method to $\gamma_1 = 0.005$, $\gamma_2 = 1/1100\gamma_1$, 5000 and $\|\mathbf{u}^{(n)} - \mathbf{u}^{(n+1)}\|_2 / \|\mathbf{u}^{(n)}\|_2 < 1.0 \times 10^{-4}$, respectively.

As shown above, we adopt CC, SAM, RMSE and ERGAS as quality measures, which are defined as follows: for $i = 1, \dots, N$ and $j = 1, \dots, B$,

$$CC(\mathbf{u}, \bar{\mathbf{u}}) = \frac{1}{B} \sum_{j=1}^B \frac{\sum_{i=1}^N (u_{i+(j-1)N} - \alpha_{\mathbf{u},j})(\bar{u}_{i+(j-1)N} - \alpha_{\bar{\mathbf{u}},j})}{\sqrt{\sum_{i=1}^N (u_{i+(j-1)N} - \alpha_{\mathbf{u},j})^2 \sum_{i=1}^N (\bar{u}_{i+(j-1)N} - \alpha_{\bar{\mathbf{u}},j})^2}},$$

$$SAM(\mathbf{u}, \bar{\mathbf{u}}) = \frac{1}{N} \sum_{i=1}^N \arccos \left(\frac{\mathbf{u}_i^\top \bar{\mathbf{u}}_i}{\|\mathbf{u}_i\|_2 \|\bar{\mathbf{u}}_i\|_2} \right),$$

$$RMSE(\mathbf{u}, \bar{\mathbf{u}}) = \frac{\|\mathbf{u} - \bar{\mathbf{u}}\|_2}{\sqrt{NB}},$$

$$ERGAS(\mathbf{u}, \bar{\mathbf{u}}) = \frac{100}{r} \sqrt{\frac{1}{B} \sum_{j=1}^B \frac{\|\mathbf{u}_j^* - \bar{\mathbf{u}}_j^*\|_2^2}{\left(\frac{1}{p} \mathbf{1}^\top \mathbf{u}_j^*\right)^{2r}}},$$

respectively, where $\mathbf{u}_i = [u_i, u_{i+N}, \dots, u_{i+(B-1)N}] \in \mathbb{R}^B$ and $\mathbf{u}_j^* = [u_{N(j-1)+1}, u_{N(j-1)+2}, \dots, u_{N(j-1)+N}] \in \mathbb{R}^N$ are the spectral and spatial vectors of \mathbf{u} , respectively, $\alpha_{\mathbf{u},j} = \sum_{i=1}^N u_{i+(j-1)N}$, $\alpha_{\bar{\mathbf{u}},j} = \sum_{i=1}^N \bar{u}_{i+(j-1)N}$ and $\mathbf{1} = [1, \dots, 1] \in \mathbb{R}^N$. Moreover, the closer CC is 1 and the smaller SAM, RMSE and ERGAS are, the more alike the estimated high HS image \mathbf{u} and the true high HS image $\bar{\mathbf{u}}$.

Table I shows CC, SAM, RMSE and ERGAS of the high HS images estimated by the existing and proposed methods ($p = 1$ or 2 in (4)) for $\sigma_2 = 0.025, 0.05$ and 0.075 . For all the quality measures and all standard deviations, one can see that the proposed method outperforms all the existing methods.

Fig. 1 plots CC, SAM, RMSE and ERGAS of the high HS images estimated by the proposed method versus λ in (3) and ω in (4), respectively, where we set $\omega = 0.01$ in the λ graphs and $\lambda = 0.03$ in the ω graphs. In CC, RMSE and ERGAS case, we found that $\lambda \in [0.02, 0.05]$ and $\omega \in [0, 0.02]$ are good choices, and HSSTV almost need not to evaluate

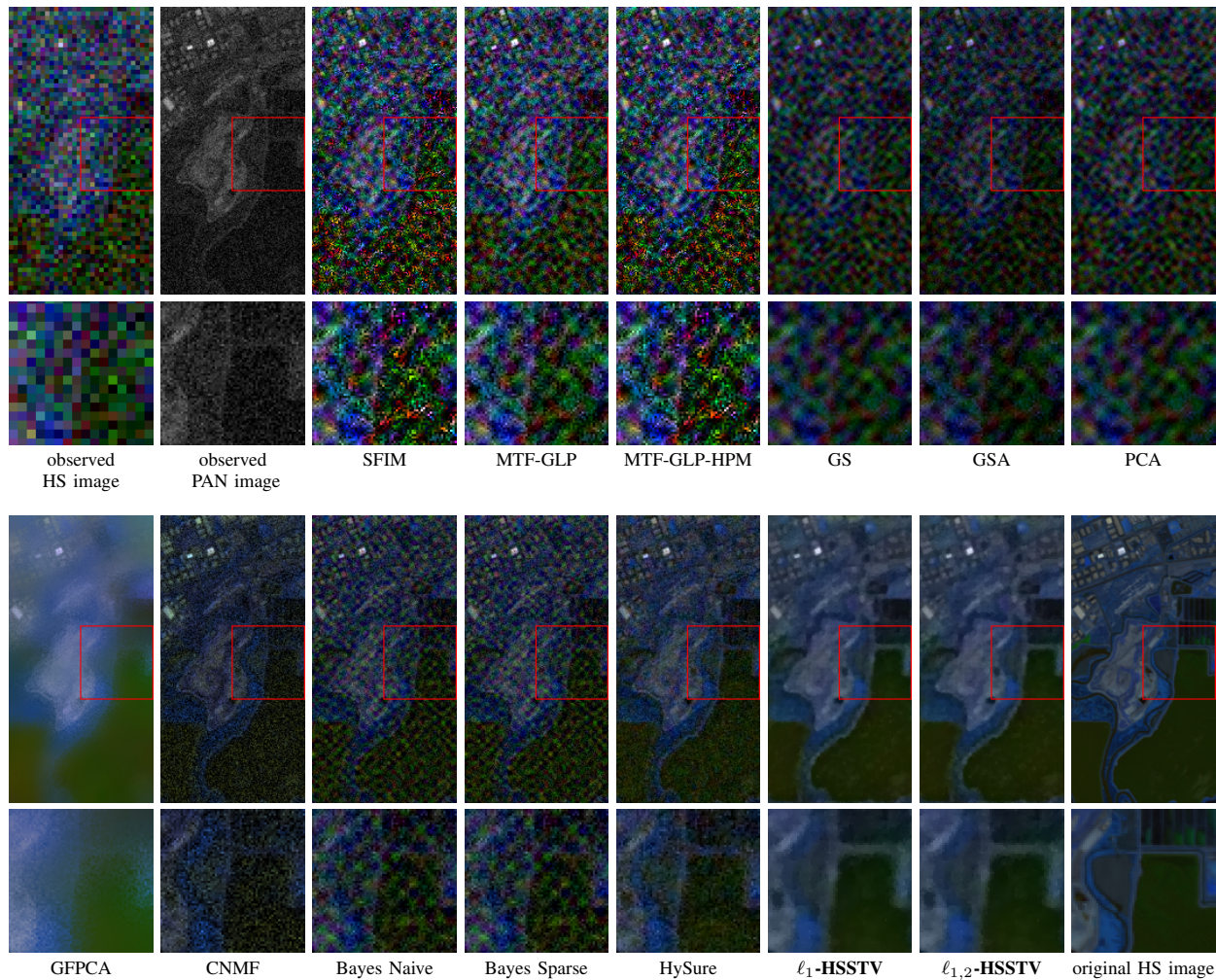


Fig. 2. Resulting HS images ($\sigma_1 = 0.1, \sigma_2 = 0.05$).

the direct spatial piecewise smoothness of an HS image in this experimental setting. This is because the second term in Prob. (3) can evaluate it not just edge similarity. For SAM case, $\lambda \in [0.06, 0.08]$ and $\omega \in [0.05, 0.08]$ are good choices.

Fig. 2 is the estimated high HS images in the $(\sigma_1, \sigma_2) = (0.1, 0.05)$ case, which depicts as RGB images (R = 16th, G = 32nd and B = 64th bands). One can see that the results estimated by most of the existing methods remain noise in the observed PAN image and include artifacts. In addition, since the color in the results by GFPCA, CNMF and HySure is different from that in the original HS image, it shows that these methods produce spectral distortion. In contrast, the proposed method can estimate the high HS image without noise, artifacts and spectral distortion, and it is most similar to the true high HS image.

IV. CONCLUSION

We have proposed a new hyperspectral panch sharpening method from a pair of noisy HS and PAN images. To consider noise in the observed PAN image, the proposed method estimates not only a high HS image but also a clean PAN image, and exploits observed information and a-priori knowledge on both the high HS image and the clean PAN image, so that it becomes robust and effective. Through our experiments, we found that the proposed method achieves better estimation than existing hyperspectral panch sharpening methods.

ACKNOWLEDGMENT

The work was partially supported by JSPS Grants-in-Aid (18J20290, 17K12710, 16K12457, 16H04362) and JST-PRESTO.

REFERENCES

- [1] C. I. Chang, *Hyperspectral imaging: techniques for spectral detection and classification*, vol. 1, Springer Science & Business Media, 2003.
- [2] A. Plaza et al., "Recent advances in techniques for hyperspectral image processing," *Remote sensing of environment*, vol. 113, pp. S110–S122, 2009.
- [3] L. Loncan, L. B. de Almeida, J. M. Bioucas-Dias, X. Briottet, J. Chanussot, N. Dobigeon, S. Fabre, W. Liao, G. A. Licciardi, M. Simoes, et al., "Hyperspectral pansharpening: A review," *IEEE Geoscience and remote sensing magazine*, vol. 3, no. 3, pp. 27–46, 2015.
- [4] N. Yokoya, C. Grohnfeldt, and J. Chanussot, "Hyperspectral and multispectral data fusion: A comparative review of the recent literature," *IEEE Geoscience and Remote Sensing Magazine*, vol. 5, no. 2, pp. 29–56, 2017.
- [5] P. Chavez, S. C. Sides, J. A. Anderson, et al., "Comparison of three different methods to merge multiresolution and multispectral data-landsat tm and spot panchromatic," *Photogrammetric Engineering and remote sensing*, vol. 57, no. 3, pp. 295–303, 1991.
- [6] W. Liao, X. Huang, F. Van Coillie, S. Gautama, et al., "Processing of multiresolution thermal hyperspectral and digital color data: Outcome of the 2014 IEEE GRSS data fusion contest," *IEEE Journal of Selected Topics in Applied Earth Observations and Remote Sensing*, vol. 8, no. 6, pp. 2984–2996, 2015.
- [7] C. A. Laben and B. V. Brower, "Process for enhancing the spatial resolution of multispectral imagery using pan-sharpening," Jan. 4 2000, US Patent 6,011,875.
- [8] B. Aiuzzi, S. Baronti, and M. Selva, "Improving component substitution pansharpening through multivariate regression of ms + pan data," *IEEE Trans. on Geosci. and Remote Sensing*, vol. 45, no. 10, pp. 3230–3239, 2007.
- [9] B. Aiuzzi, L. Alparone, S. Baronti, A. Garzelli, and M. Selva, "Mtf-tailored multiscale fusion of high-resolution ms and pan imagery," *Photogrammetric Engineering & Remote Sensing*, vol. 72, no. 5, pp. 591–596, 2006.
- [10] G. Vivone, R. Restaino, M. Dalla Mura, G. Licciardi, and J. Chanussot, "Contrast and error-based fusion schemes for multispectral image pansharpening," *IEEE Geoscience and Remote Sensing Letters*, vol. 11, no. 5, pp. 930–934, 2014.
- [11] J. G. Liu, "Smoothing filter-based intensity modulation: A spectral preserve image fusion technique for improving spatial details," *International Journal of Remote Sensing*, vol. 21, no. 18, pp. 3461–3472, 2000.
- [12] R. C. Hardie, M. T. Eismann, and G. L. Wilson, "Map estimation for hyperspectral image resolution enhancement using an auxiliary sensor," *IEEE Trans. Image Process.*, vol. 13, no. 9, pp. 1174 – 1184, 2004.
- [13] Q. Wei, J. Bioucas-Dias, N. Dobigeon, and J. Y. Tourneret, "Hyperspectral and multispectral image fusion based on a sparse representation," *IEEE Trans. on Geosci. and Remote Sensing*, vol. 53, no. 7, pp. 3658 – 3668, 2015.
- [14] M. Simões, J. Bioucas-Dias, L. B. Almeida, and J. Chanussot, "A convex formulation for hyperspectral image superresolution via subspace-based regularization," *IEEE Trans. on Geosci. and Remote Sensing*, vol. 53, no. 6, pp. 3373–3388, 2015.
- [15] N. Yokoya, T. Yairi, and A. Iwasaki, "Coupled nonnegative matrix factorization unmixing for hyperspectral and multispectral data fusion," *IEEE Trans. on Geosci. and Remote Sensing*, vol. 50, no. 2, pp. 528–537, 2012.
- [16] S. Takeyama, S. Ono, and I. Kumazawa, "Robust and effective hyperspectral pansharpening using spatio-spectral total variation," *Proc. IEEE Int. Conf. Acoust., Speech, Signal Process. (ICASSP)*, pp. 1603–1607, 2018.
- [17] A. Chambolle and T. Pock, "A first-order primal-dual algorithm for convex problems with applications to imaging," *J. Math. Imaging and Vision*, vol. 40, no. 1, pp. 120–145, 2010.
- [18] E. Y. Sidky, J. H. Jørgensen, and X. Pan, "Convex optimization problem prototyping for image reconstruction in computed tomography with the chambolle-pock algorithm," *Physics in medicine and biology*, vol. 57, no. 10, pp. 3065, 2012.
- [19] C. Sutour, C.-A. Deledalle, and J.-F. Aujol, "Adaptive regularization of the nl-means: Application to image and video denoising," *IEEE Trans. Image Process.*, vol. 23, no. 8, pp. 3506–3521, 2014.
- [20] S. Ono and I. Yamada, "Decorrelated vectorial total variation," in *Proc. IEEE Conf. Comput. Vis. Pattern Recognit. (CVPR)*, 2014.
- [21] S. Ono, "Primal-dual plug-and-play image restoration," *IEEE Signal Process. Lett.*, vol. 24, no. 8, pp. 1108–1112, 2017.
- [22] S. Takeyama, S. Ono, and I. Kumazawa, "Hyperspectral image restoration by hybrid spatio-spectral total variation," *Proc. IEEE Int. Conf. Acoust., Speech, Signal Process. (ICASSP)*, pp. 4586–4590, 2017.
- [23] C. Chen, Y. Li, W. Liu, and J. Huang, "Image fusion with local spectral consistency and dynamic gradient sparsity," in *Proc. IEEE Conf. Comput. Vis. Pattern Recognit. (CVPR)*, 2014, pp. 2760–2765.
- [24] M. Afonso, J. Bioucas-Dias, and M. Figueiredo, "An augmented Lagrangian approach to the constrained optimization formulation of imaging inverse problems," *IEEE Trans. Image Process.*, vol. 20, no. 3, pp. 681–695, 2011.
- [25] G. Chierchia, N. Pustelnik, J.-C. Pesquet, and B. Pesquet-Popescu, "Epi-graphical projection and proximal tools for solving constrained convex optimization problems," *Signal, Image and Video Process.*, pp. 1–13, 2014.
- [26] S. Ono and I. Yamada, "Signal recovery with certain involved convex data-fidelity constraints," *IEEE Trans. Signal Process.*, vol. 63, no. 22, pp. 6149–6163, 2015.
- [27] S. Ono, " L_0 gradient projection," *IEEE Trans. Image Process.*, vol. 26, no. 4, pp. 1554–1564, 2017.
- [28] J. J. Moreau, "Fonctions convexes duales et points proximaux dans un espace hilbertien," *C. R. Acad. Sci. Paris Ser. A Math.*, vol. 255, pp. 2897–2899, 1962.
- [29] H. H. Bauschke and P. L. Combettes, *Convex analysis and monotone operator theory in Hilbert spaces*, Springer, New York, 2011.
- [30] F.A. Kruse, A.B. Lefkoff, J.W. Boardman, K.B. Heidebrecht, A.T. Shapiro, P.J. Barloon, and A.F.H. Goetz, "The spectral image processing system (SIPS)—interactive visualization and analysis of imaging spectrometer data," *Remote Sensing of Environment*, vol. 44, no. 2, pp. 145–163, 1993.
- [31] L. Wald, "Quality of high resolution synthesised images: Is there a simple criterion?," in *Third conference "Fusion of Earth data: merging point measurements, raster maps and remotely sensed images"*, 2000, pp. 99–103.
- [32] L. Wald, T. Ranchin, and M. Mangolini, "Fusion of satellite images of different spatial resolutions: Assessing the quality of resulting images," *Photogrammetric Engineering & Remote Sensing*, vol. 63, no. 6, pp. 691–699, 1997.